Journal of Atmospheric and Solar-Terrestrial Physics 70 (2008) 2336–2345

Contents lists available at ScienceDirect

Journal of Atmospheric and Solar-Terrestrial Physics

journal homepage: www.elsevier.com/locate/jastp

Relation of auroral substorm onset to local AL index and dispersionless particle injections

James M. Weygand [a,*], R.L McPherron [a], K. Kauristie [b], H.U. Frey [c], T.-S. Hsu [a]

[a] Institute of Geophysics and Planetary Physics, University of California, Los Angeles, CA, USA
[b] Finnish Meteorological Institute, Space Physics Program, Finland
[c] Space Sciences Laboratory, University of California, Berkeley, CA, USA

ARTICLE INFO

Article history:
Accepted 24 September 2008
Available online 19 October 2008

Keywords:
Substorm
AL index
Timing
Dispersionless injections

ABSTRACT

In this study, we investigate the relation of auroral substorm onset to the sharp decrease in the local AL index (IL) during substorms. With a database of over 4200 onsets determined from auroral images, we have statistically examined the timing between the auroral substorm onset and the sharp decrease in the IL index, as determined with data from the IMAGE magnetometer network. From the database of onsets, 54 substorms were determined to be within 6° of the central meridian of the IMAGE ground array. Our superposed epoch median curve shows that the IL index begins to sharply decrease 3 min before the auroral onset, which is twice the 2 min resolution of the auroral imager. However, the mean difference determined by measuring the time between the start of the IL decrease and the auroral substorm onset is about 1.1 ± 0.6 min. An analysis of the superposed epoch median curves of the SOPA particle data for the LANL spacecraft closest to the auroral onset meridian indicates that both the electron and proton injections begin about 3 min before the auroral onset. However, the mean time of the difference between the minimum of the particle dispersionless injection and the auroral onset is simultaneous within the uncertainty of the auroral onset and the error of the mean for the injection. The location of the electron injection relative to the IMAGE ground array seems to be 01–04 MLT, while the proton injection appears to be in the 22–01 MLT sector. These statistical results support the idea that the field aligned and ionospheric currents of the substorm current wedge begin to flow before the auroral onset.

1. Introduction

The methods used to determine substorm onset time include analysis of auroral images, geomagnetic indices, Pi 2 pulsations, dipolarization of the geosynchronous magnetic field, and geosynchronous particle injections. Spacecraft auroral images are typically considered to be one of the most reliable methods of identifying substorm events; however, the exact time of onset is normally difficult to identify due to the limited temporal resolution of most auroral images. With the auroral electrojet (AL) index the substorm onset determination involves identifying the beginning of a sharp decrease in the AL index. McPherron et al. (1986) noted that the AL currents begin to strengthen during the growth phase before the auroral substorm onset time, although, only a qualitative description was given. Pi 2 pulsations and dipolarizations of the magnetic field observed by GOES are two other means of identifying substorm onset time. Liou et al. (1999, 2000, 2002) found that 65% of the Pi 2 pulsations begin about 0–3 min after the start of the auroral breakup identified with the Polar ultraviolet images, while the GOES satellites observed dipolarizations 1.7 ± 2.7 min after this time. The most probable location of the geosynchronous location of this

* Corresponding author.
E-mail address: jweygand@igpp.ucla.edu (J.M. Weygand).

1364-6826/$ - see front matter © 2008 Elsevier Ltd. All rights reserved.
doi:10.1016/j.jastp.2008.09.030

dipolarization was found to be about 23 MLT (Cai et al., 2006). When the Pi 2 pulsations were compared with the standard AL index, Hsu and McPherron (2003) and Hsu and McPherron (2007) indicate that there is no clear relationship between the start of the Pi 2 pulsations and the AL index. They further state the AL index is not always ideal for identifying substorm events. This finding is supported by Sakurai and Saito (1976) who found that Pi 2 pulsations are more sensitive to small substorms than the AE index. However, Meng and Liou (2002) found in a study using 28 events that the auroral onset often precedes the quick-look AE index onset by 3.6 ± 4.8 min.

The dispersionless injection of electrons and protons at the geosynchronous orbit observed by the Los Alamos National Laboratory (LANL) SOPA instrument is another method used to identify substorm onsets. The dispersionless particle injection is considered one of the more reliable indicators of substorm onset; however, dispersionless injections have also been observed during pseudo breakups (Koskinen et al., 1993; Nakamura et al., 1994; Pulkkinen et al., 1998), and not normally during poleward boundary intensifications (PBIs) (Zesta et al., 2002), but they have been observed with north–south aligned PBIs (Henderson et al., 1994; Sergeev et al., 1999). Liou et al. (2001) previously examined statistically the difference between the auroral breakup time and the start of dispersionless injection and found that for 34 events the injection time at the LANL spacecraft relative to the start of the auroral breakups varied from −2 to +8 min with an average lag of 1.8 min and a standard deviation of 2.5 min. From these results they concluded that the particle energization takes place about 1 min before the auroral onset. To further complicate matters, Birn et al. (1997) have shown that dispersionless ion injection can occur before the electron injection, at the same time as the electron injection, or after the electron injection when injections are seen in both types of particles. Statistically the particles are ions when the spacecraft is pre-midnight and electrons when it is post-midnight. They have also demonstrated that those injections frequently occur in only one type of particle. However, multi-spacecraft studies have shown that electron only and ion only signatures recorded at one spacecraft can be observed for events that actually inject both species as observed at another spacecraft (Reeves et al., 1990). Finally, with respect to the dispersionless injection, the sharp AL index decrease has been previously observed before and after the dispersionless injection (Reeves et al., 1992; Reeves, GEM talk, 1997).

The preceding discussion demonstrates that a number of methods exist for identifying the substorm onset and that there are differences in the start times relative to the auroral substorm onset determined by these different methods. None of these methods is 100% reliable in the determination of substorm onset times. However, in this work we study the relation between these various phenomena using the best available datasets. We began with a list of over 4200 auroral brightenings observed by the Imager of Magnetopause-to-Aurora Global Exploration (IMAGE) spacecraft (Frey et al., 2004; Frey and Mende, 2006). From this list we selected 54 substorm onsets that occurred within 6° of the center of the International Monitor for Auroral Geomagnetic Effects (IMAGE) ground magnetometer array. For this subset of events we produced a local AL index at 10 s resolution that monitors all changes in the strength of the westward electrojet over the array. Also, for this subset we acquired high time resolution synchronous particle data from the LANL SOPA detectors. We will show that intensification of the westward electrojet and the dispersionless particle injection begins about the same time as the auroral brightening within the uncertainty of the averages.

2. Instrumentation and data

Data from the IMAGE spacecraft, the IMAGE ground magnetometer array, and LANL spacecraft are used in this study. Auroral images used to identify substorm onsets were obtained by the IMAGE far ultraviolet photon imager, which has a temporal resolution of about 2 min. All of the substorm onsets used in this study were identified with the procedure described in Frey et al. (2004); and Frey and Mende (2006) by looking at WIC images because their spatial resolution is better than images produced by the SI-12 and SI-13 imagers. When WIC images did not provide an adequate view of the auroral oval the SI-13 images were used instead.

The onsets in the Frey et al. study satisfied the following criteria: (1) a clear local sudden brightening of the aurora, (2) the aurora subsequently expanded poleward of the auroral oval and spread azimuthally in local time for at least 20 min, and (3) 30 min had to pass between substorm onsets for each to be considered a separate event. Fig. 1 displays a good example of a substorm onset at 1948:05 UT on September 25, 2000, which meets these criteria. The purpose of criteria 2 and 3 is to eliminate pseudo-breakups, PBIs, and multi-onset substorms from this study. Approximately 4200 substorms were observed during the IMAGE mission. Of these, 75 auroral onsets occurred within 6° longitude of the central line of the IMAGE magnetometer array running from about Ny Ålesund (NAL) to Oulujärvi (OUJ). The choice of $\pm 6°$ in longitude is arbitrary.

The10-s resolution local AL (IL) index employed in this study was constructed from the IMAGE array of ground magnetometers (Kauristie et al., 1996). The procedure used is similar to that used in the construction of the standard AE indices. First a background level is determined for each station in the array. This level is defined as a quiet interval on the order of 0.5–2 h long of the same day or the next closest day if the geomagnetic activity is high. Here "quiet" is defined as the interval with the smallest difference between the maximum and minimum H value. The H component of the stations are superposed after subtracting the baselines and the lower envelope of the curves is taken as the IL index while the upper envelope gives the IU indices. Ten second resolution IL data are produced in order to reduce the uncertainty between the observed auroral brightening time and the sharp decrease in the IL index. The resolution of the IL index is limited to 10 s due to the resolution of some of the IMAGE ground magnetometers.

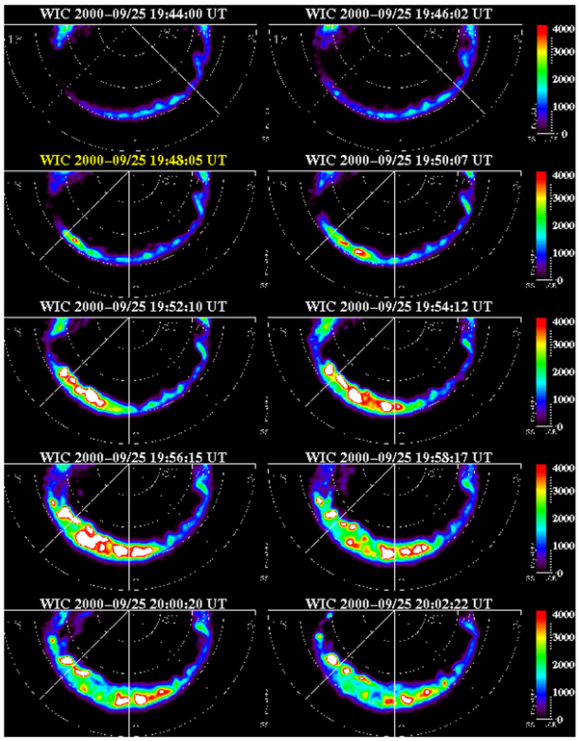

Fig. 1. Sequence of processed IMAGE WIC auroral images of the September 25, 2000 substorm onset at 1948:05 UT (second image from the top in the first column with the time in yellow). These images have been projected on a two-dimensional plane tangent to the north magnetic pole.

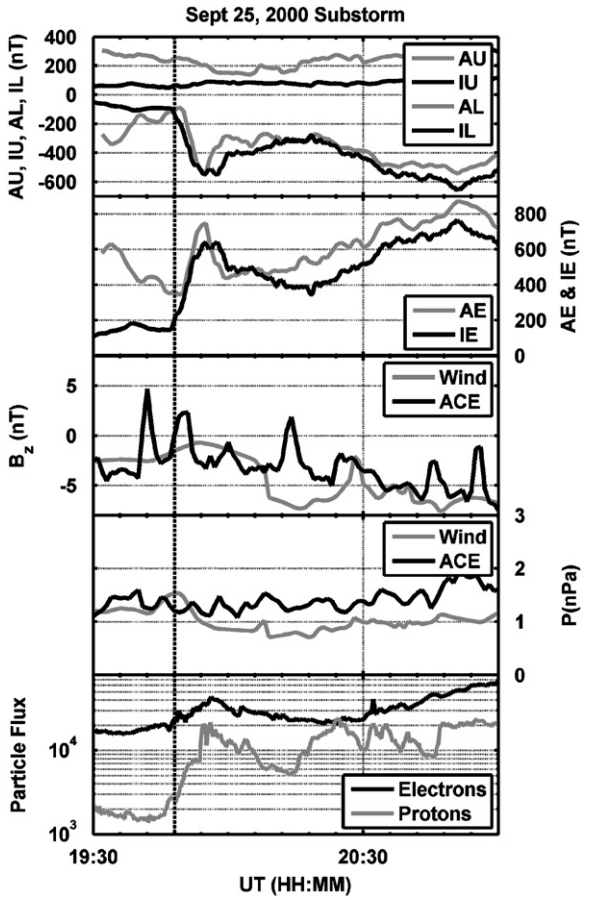

Fig. 2. Local auroral electrojet indices (black) and AE indices (gray), propagated IMF B_z and solar wind dynamic pressure, and LANL SOPA electron and proton fluxes from the second energy channel for the September 25, 2000 auroral onset. The auroral onset time is indicated with the dashed vertical line. Both the Wind and ACE data are shown for this event.

Of the 75 substorm onsets that occurred within about 6° of the IMAGE ground magnetometer array only 54 displayed a sharp decrease in the IL index exceeding −50 nT within 15 min of the IMAGE spacecraft onset observation. Fourteen of the 75 events were identified as pseudo breakups because no IL decrease was observed or the ground magnetometer data of the individual stations show a localized negative H component change that recovers in a few minutes. Seven events were determined to be PBIs because no midlatitude Pi 2 were observed and the auroral onset occurred at the poleward edge of the auroral oval.

The LANL SOPA data were employed to identify simultaneous particle injection at the geosynchronous orbit. The particle injections are a simultaneous enhancement in particle fluxes over a broad range of energies from 50 keV to as high as 200 keV (Reeves and Henderson, 2001). Particle injections can occur in the electrons, ions, or both (Birn et al., 1997).

This study also uses solar wind magnetic field and dynamic pressure data. These data were propagated from the original position of the ACE, Wind, or Geotail spacecraft (i.e., whichever spacecraft had available solar wind data) to the nominal subsolar bow shock at (17, 0, 0) R_E using the modified-minimum variance technique outlined in Weimer (2004) and Weimer et al. (2002, 2003).

Fig. 2 displays the local electrojet indices, AE indices, and solar wind data associated with the substorm shown in Fig. 1. The IL and IU indices are plotted in the top panel in black and the AE indices are plotted in gray. The IE index shows a slight increase of about 35 nT at about 1948 UT in the IU index caused by an intensification of the eastward electrojet, and a sharp decrease in the IL index caused by an intensification of the westward electrojet. The AE index displays a decrease in the AU index and a sharp decrease in the AL index at about 1949 UT. The vertical dashed line in the figure indicates the time of the substorm onset as determined from the auroral images. The second panel gives the IE index that also shows the sharp increase at the time of the substorm onset. The third and forth panels display the solar wind IMF and dynamic pressure as observed by both ACE located at (230, −36, −1) R_E GSE (black curve) and Wind at (35, −250, −6) R_E GSE (gray curve) spacecraft. The considerable difference in the solar wind plasma and IMF data observed by ACE and Wind is most likely related to their large separation along both the x and y axes. Ridley (2000) found that the correlation coefficient significantly decreased for separations along the y axis larger than $30R_E$ for all the

propagation methods examined in their study. Similar decreases in the correlation coefficient have been observed for the Weimer (2004) and Weimer et al. (2003) method. The bottom panel presents the LANL SOPA data from spacecraft 1991-080 for this event. The simultaneous dispersionless injection of electrons and ions begins at about 1946 UT.

3. Analysis

Fig. 3 displays results of a superposed epoch analysis of a three-point derivative of the IL and AL indices, the local electrojet and the AE indices, solar wind IMF, and LANL spacecraft electron and proton flux injection data for the substorm onsets that occurred relatively close (i.e., within about 20° longitude due to the fixed location of the LANL spacecraft) to the meridian of the IMAGE ground array. The solid black and gray curves are the median of the events for the local indices and the AE indices, respectively. The epoch zero time is the substorm onset time as identified in the auroral images. The first panel of this figure shows the median behavior of a three-point derivative of the IL index for all events. The median curve demonstrates that the slope of the IL index begins to change about 3 min before the auroral onset. Note that the three-point derivative of the AL index shows no similar peak in the data. The second and third panels also demonstrate that the decrease in the IL index and an increase in the IE begin about 3 min before the auroral onset time. The fourth panel displays the superposed epoch results for the solar wind IMF B_z. The median B_z component becomes negative about 2.5 h before epoch zero (not shown) and begins to gradually increase for about 15 min after epoch zero. The superposed curve of the solar wind dynamic pressure (not shown) displays little to no change before and after epoch zero. The bottom panel of Fig. 3 presents superposed epoch curves for the LANL SOPA electron and proton fluxes. All the injections included in this superposed epoch consist of dispersionless injections. Only the medians of the first five energy channels for the electrons (50–315 keV) and protons (50–400 keV) are plotted. The fluxes recorded in the second through fifth energy channel have been multiplied by constant factors to group the curves closer together and more clearly show the injection. It should be noted that these superposed epoch curves include only 29 of the 54 events that had dispersionless injections. Events where no dispersionless injection was observed were not included to more clearly show the particle flux dispersionless injection. It is likely that the LANL spacecrafts were not properly located for the other 25 onsets, or particle injections did not penetrate to synchronous orbit.

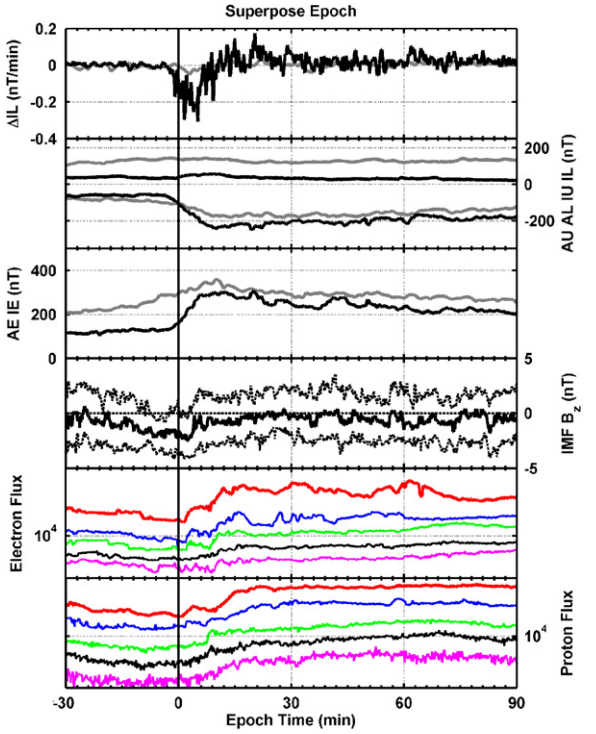

Fig. 3. Superposed epoch of the three-point derivative of the IL index, local and standard auroral electrojet indices, IMF B_z, and LANL SOPA electron and proton fluxes for the auroral onsets in this study. The solid black and gray curves in the first three panels are the median of the events for the IL and the AE indices, respectively. In the fourth panel the bold black curve is the median of 54 auroral onsets and the dashed curves are the upper and lower quartiles. The bold vertical line marks epoch time zero. In the bottom two panels only the first five energy channels are shown and the higher energy channels have been multiplied by a constant factor to better display the curves.

One weakness of the superposed epoch method is large events can dominate the results. Fig. 4 shows a histogram of time differences between the auroral substorm onset and the sharp drop in the IL index. The time differences were determined by examining the individual events. The mean and median of this histogram are 1.1 and 1 min, respectively, before the auroral onset and the standard deviation is 4.0 min and the error of the mean is 0.6 min. The figure demonstrates two points. The first point is that some large events are dominating the sharp decrease

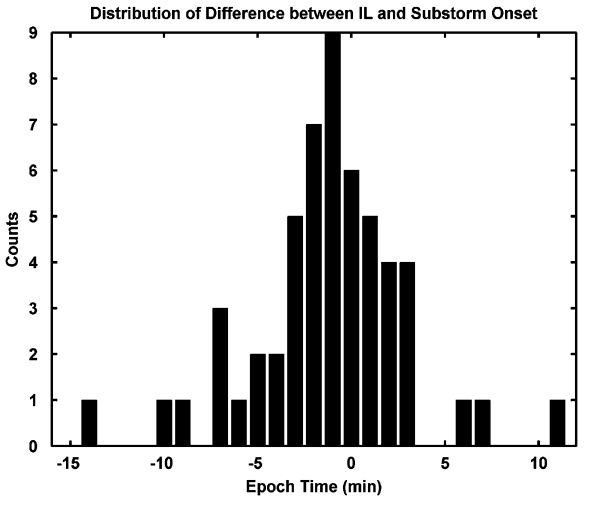

Fig. 4. Histogram of the difference between the auroral onset time and the start of the sharp drop in the IL index. The histogram peaks at 1 min before the auroral onset time.

observed in the superposed epoch of the IL index. Secondly, the sharp decrease in the IL index is simultaneous within the 2 min resolution of the auroral images.

Fig. 3 shows a superposed epoch curve made from 29 different auroral onsets with data from only one LANL spacecraft per auroral onset. However, for each of these auroral onsets data from as many as six LANL spacecrafts are available at other local times. Not all of the LANL spacecraft recorded a dispersionless injection. Fig. 5 shows the superposed LANL particle data from all available LANL spacecraft binned according to MLT for 29 of the auroral onset events discussed in Fig. 3. Due to the limited amount of data the MLT bins are each 3 h and the bins have been selected such that the mean location of the substorm auroral onset (about 23 MLT (Frey et al., 2004)) and local midnight are within the same bin. This figure indicates where in MLT the particle injects occur. In each panel the black curve shows the median of the lowest energy electron flux channel and the gray curve shows the lowest proton flux channel. For many of the auroral onsets data from multiple LANL spacecrafts were available, but typically only one or two show the dispersionless injections. Many other bins include dispersed injections. Note that for the fourth (10–23 MLT), fifth (13–16 MLT), and sixth panels (16–19 MLT) little to no electron and ion data were available. In the top panel the electron injection appears to begin about 3 min before the auroral onset and the ion injection begins about 3 min before the auroral onset in the bottom panel. An increase in the particle flux is also apparent in panels 2 and 7 and all of these increases appear to start about the same time as the auroral onset or after the auroral onset.

Fig. 6 shows the superposed LANL particle data from all the available LANL spacecraft located at different local times with respect to the position of the IMAGE ground array and we refer to these bins as IMAGE local time (ILT). For this figure, we treat the IMAGE ground array always as epoch local time zero (00 ILT). The purpose of this figure is to demonstrate where the particle injections occur with respect to the auroral onset location since all of the auroral onsets occur directly above the IMAGE ground array. In Fig. 6 the same energy channels are used and gray curve indicates the protons and black curve for the electrons. Similar to Fig. 5, multiple LANL spacecraft data were available for many of the auroral onsets and typically several show the dispersionless injections, while many

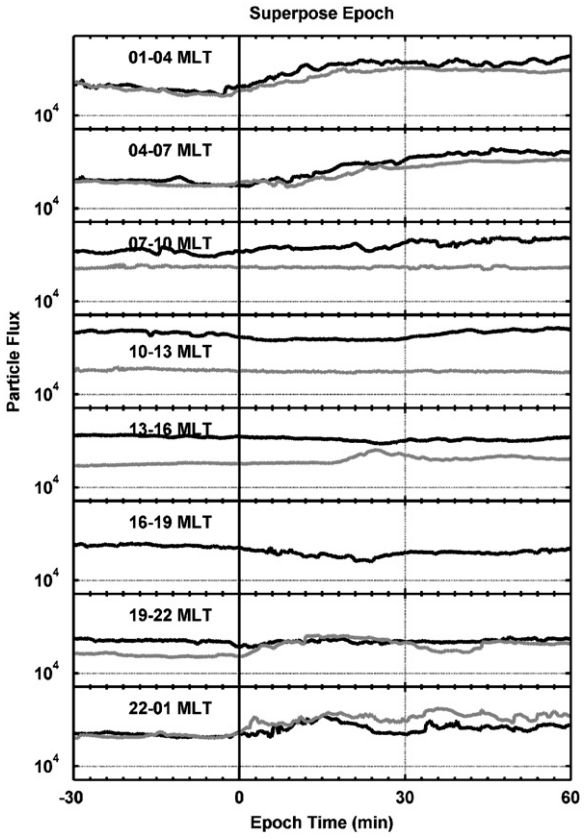

Fig. 5. Superposed epoch curves for binned LANL SOPA electron fluxes for 29 auroral onset events that displayed a dispersionless particle injection. The solid black and gray curves are the median of the events for the electrons and the protons, respectively. The bold vertical line marks epoch time zero. These data are binned by MLT for 3 h bins, the MLT range for each bin is given in each panel.

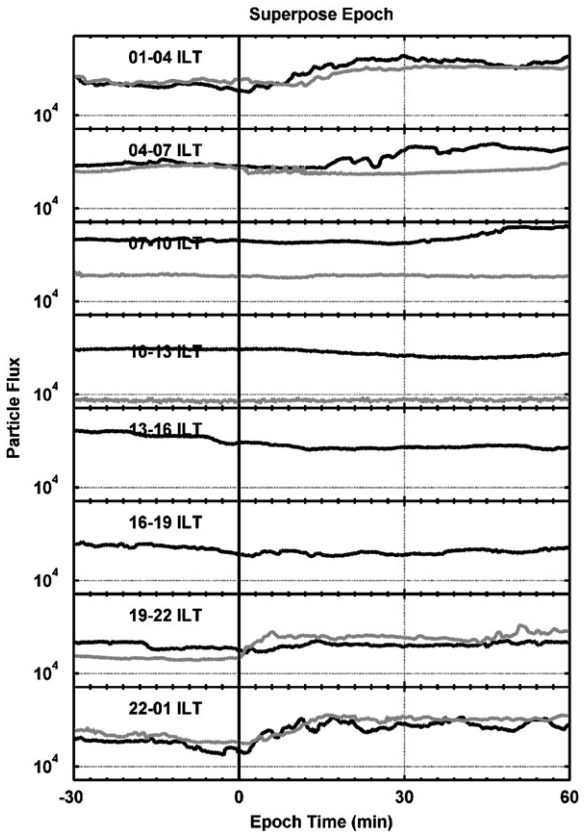

Fig. 6. Superposed epoch curves for binned LANL SOPA electron fluxes for 29 auroral onset events that displayed a dispersionless particle injection. The solid black and gray curves are the median of the events for the electrons and the protons, respectively. The bold vertical line marks epoch time zero. For this figure the data are binned with respect to the location of the IMAGE ground array where the IMAGE array is at 00 ILT. The ILT range for each bin is given in each panel.

other bins include dispersed injections. The ILT bin size is indicated in each panel. Note that for the fourth (10–23 ILT), fifth (13–16 ILT), and sixth panels (16–19 ILT) electron and ion data were either not readily available or limited. The first panel indicates that the electron flux injection begins about 1–2 min after the auroral onset, while the last panel shows the electron flux injection occurs at about the same time as the auroral onset. The second panel also seems to show some injection, but this is not as clear as in the first and last panels. The sharpest particle change is present in the last panel and suggests that the mean location for the electron flux injection associated with the auroral onsets used in this study is in the 22–01 ILT sector and in the same bin as the IMAGE ground array.

The most pronounced changes in the ion fluxes occur in the 19–22 and the 22–01 ILT bin. The ion fluxes in the 19–22 ILT bin appear to increase about the same time as the auroral onset. The injection in the last panel appears to begin about 2–3 min after the auroral onset. The seventh and eighth panels show that the ion injection occurs closer to the dusk than the electron injections, which are clearest in the 22–01 and the 01–04 ILT bin. In other words, the ion and electron injections appear to be partially offset from one another in local time.

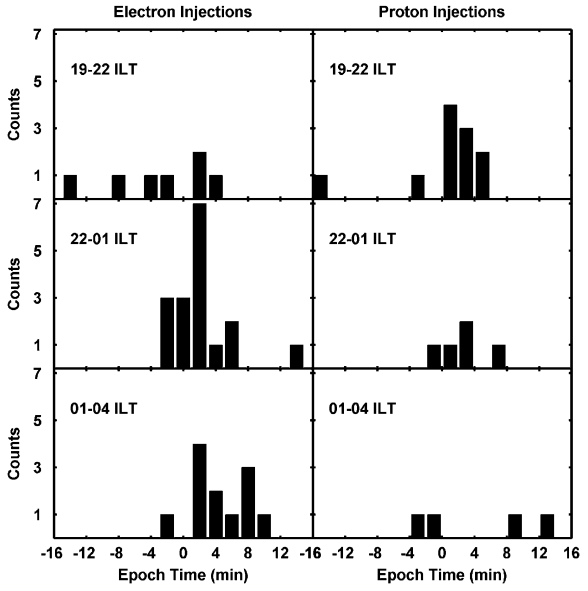

Fig. 7. Histogram of the difference in time between the particle dispersionless injection and the auroral onset binned by ILT. Negative values indicate the injection begins before the auroral onset. The left column contains the electron injection information and the right column displays the proton injection time differences.

As we discussed for Fig. 4, large events can dominate the results in the superposed epoch method. Fig. 7 shows a histogram of time differences between the auroral substorm onset and the electron (left column) and proton (right column) dispersionless injections in the SOPA data for the 19–22, 22–01, and 01–04 ILT bins. The other ILT bins are not shown because of the lack or absence of dispersionless injections observed in those bins. The results for histograms for the MLT bins are not given because they provide no additional information. The time differences were determined by examining the individual events, and the minimum in the particle fluxes was identified as the start of the injection. The mean and the error of the mean for the differences in time between the particle dispersionless injections and the auroral onsets are given in Table 1. The figure demonstrates two points. The first point is that some large events are dominating the injections observed in the superposed epoch of the LANL SOPA fluxes. Secondly, the mean injection time relative to the auroral onset time varies with the local time bin.

4. Discussion and conclusions

In this study, we constructed superposed epoch curves of the local electrojet indices, which demonstrate features that have been shown with a number of individual cases (Hsu and McPherron, 2003), but not with a significant statistical database. The curves show that the westward electrojets begin to strengthen about 3–4 min before the auroral onset. However, this early increase in strength appears to be the result of a bias created by several large events. When we examine the histogram of the differences between the IL decrease and the auroral image onset in Fig. 4, we obtain an asymmetrical distribution with peak probability of the IL decrease about 1 min before the auroral onset. We note that the auroral imager obtains an image approximately every 2 min, which means that the change in the local electrojet indices 1 min before the auroral onset would be simultaneous within the resolution of the imager. However, we point out that there are some studies, including this study, which show individual events with the AL index decreasing before and after the auroral image onset (Liou et al., 2003). It could be argued that this delayed decrease in the

Table 1
Mean difference in time between the particle dispersionless injection observed in the first energy channel (about 50–75 keV) of the SOPA instrument and the auroral onset

Local time Bin	Electrons MLT (min)	Protons MLT (min)	Electrons ILT (min)	Protons ILT (min)
19–22	-3.9 ± 1.4	$+0.7\pm1.1$	-3.1 ± 2.4	-0.6 ± 1.7
22–01	-0.1 ± 1.8	-1.9 ± 3.0	$+2.2\pm0.9$	$+4.2\pm2.9$
01–04	$+2.4\pm1.0$	$+4.4\pm2.5$	$+4.3\pm1.0$	$+3.9\pm3.7$

The uncertainty is the error of the mean. Negative values mean the injection occurred before the auroral onset and positive values for after the auroral onset.

AL index after the auroral onset is the result of the large local time separation between the ground magnetometer location used in AE determination and the auroral onset location, but even in our study several decreases in the IL index began after the auroral image onset. The observations of a decrease well before the auroral onset, such 10–15 min before, could be the result of a poorly identified auroral onset time.

The observation of the IL decrease at about the same time as the auroral onset suggests that the substorm current wedge has formed just before or at the same time as the UV observation of the onset. This makes physical sense if the upward field-aligned current in the substorm current wedge is the cause of the auroral onset as is generally believed (Atkinson, 1967; McPherron et al., 1973; Angelopoulos, 2008). In order for the onset brightening to become visible to the imager the field-aligned potential difference has to increase, which results in the enhanced field-aligned currents. This increased potential difference most likely follows enhanced magnetospheric convection in the magnetotail during southward IMF.

An alternative explanation is that a decrease in IL is caused by enhancement in the ionospheric conductances in a limited nightside MLT sector. This conductance enhancement could be caused by those precipitating particles in the field-aligned current associated with the Harang discontinuity, but these particle fluxes are not sufficiently intense to produce auroras visible to the imagers because they have not yet gained enough energy through field-aligned acceleration. Thus, what may happen is at the western edge of the wedge area a sharp conductance gradient forms and a charge builds up, but in the corresponding magnetospheric region there are not enough current carriers. The field-aligned potential drop then increases and the precipitating particles gain enough energy to produce strong field-aligned currents and auroras visible to the imagers.

The results of this study are within the uncertainty of those finding in Meng and Liou (2002) who used 28 events to find that the quick-look AE onset was delayed by 3.6 ± 4.8 min. A direct comparison between that study and this one is difficult for several reasons. First, it is unclear whether there is at least one AE ground station below each of the auroral onsets. Secondly, it is not clear how the Meng and Liou study define an auroral onset. The example shown in their study meets the criteria of substorm according to Frey et al. (2004) and Frey and Mende (2006), but it has been shown in several studies that not all the Frey et al. (2004) and Frey and Mende(2006) events are auroral substorm onsets (Weygand et al., 2008). However, Fig. 3 of our paper displays the results of the superposed epoch for the standard AL index (see the lower gray curve in the second panel). This plot shows a decrease in AL with about the same magnitude, but the decrease begins earlier and is more gradual than the one observed in the IL index. According to the superposed epoch curve for the AL index the decrease would begin well before the auroral onset, which disagrees with Meng and Liou (2002). Why the AL index observes an earlier decrease is not clear at this time, but it may be due to preceding pseudo breakups.

We also observed in Fig. 3 that the median IMF B_z curve was negative for 1 h before and after the epoch zero time, but there is a small increase of about 1 nT about 15 min after the epoch zero time. This small change in the B_z component could be the result of averaging together substorms that have been triggered, which is about 60% of substorms, and those that have not been triggered, which is about 40% of substorms (Hsu and McPherron, 2003). However, the increase in the B_z component about 15 min after the auroral onset time is troubling since Hsu and McPherron (2003) show that most of the IMF B_z substorm triggers come within 10 min of the auroral onset time. The northward turning of the B_z component might also be the result of averaging together many solar wind intervals, but an examination of the propagated IMF B_z component of the superposed epoch of the original 4200 auroral onsets indicates that the northward turning of the B_z component occurs about 25 min before the epoch zero time. Furthermore, it is interesting to note that the magnitude of the northward turning in the superposed epoch analysis of the 4200 onsets is approximately the same. If we were to believe that all substorms have a northward turning before the substorm onset, but a northward turning is not observed in the median superpose epoch of B_z for the subset of 54 onsets, then one might believe that the subset of 54 onsets may be composed mainly of pseudo breakups, which are not generally associated with a northward turning of B_z. Therefore if we believe our subset of 54 onsets is mostly pseudo breakups, then it indicates that the line between pseudo breakups and substorms is unclear since all of the subset of 54 auroral onsets show the characteristic substorm sudden brightening followed by a poleward and azimuthal expansion of the substorm expansion phase.

The bottom two panels of Fig. 3 also display a superposed epoch of the LANL SOPA electron and protons fluxes for only those LANL SOPA fluxes that displayed an injection. The curves for most of the energy channels show a decrease in the flux related to the stretching of the magnetic field lines followed by an increase in both the electrons and proton fluxes, which indicates that an injection of fluxes has occurred. However, the exact time at which the injection begins is unclear due to the gradual change in the curves. The start of the injection appears to be easier to identify in the top and bottom panels of Figs. 5 and 6. In these figures both the electron and proton fluxes for the first energy channel are in the same panel. The data for 29 substorms, which show an injection in at least one spacecraft, have been binned by MLT location in Fig. 5 and by ILT location in Fig. 6 using all the available LANL spacecraft. First, we will consider the superposed epoch curves in Fig. 5. In this figure the electron and proton dispersionless injections appear to begin about 3–4 min before the auroral onset in the 01–04 and 22–01 MLT bins, respectively. Electron injections also appear to be present in the 04–07 MLT bin and possiblly the 22–01 MLT bin and these occur after the auroral onset. Proton injections are also visible in the 01–04 and 19–22 MLT bin and these occur after the injection in the 22–01 MLT bin and about the same time as the auroral onset in the 19–22 MLT bin. The differences in the start time of the injections in the

different MLT bins are most likely due to a propagation effect. The question remains whether the electron and proton dispersionless injections observed before the auroral onset in the superposed epoch are real. The second column in Table 1 shows that for the most part the superposed epoch curve of the proton injection before the auroral onset is most likely the results of one or two cases dominating the superposed epoch and the error of the mean indicates that the proton injection occurs statistically at the same time as the auroral onset. In the 22–01 and 01–04 MLT electron bins (first column of Table 1) the electron dispersionless injection also occur statistically at the same time as the auroral onset. Only in the 19–22 MLT bin of Table 1 does the electron dispersionless injection mean value occur before the auroral onset, but only four events contribute to the mean. Thus, it is likely that a few events in the 01–04 MLT bin influence the dispersionless injection observed 3 min before the auroral onset in the first panel of Fig. 5.

Another relevant point determined by Liou et al. (2001) was that the dispersionless injections were found to be ± 1 h in MLT from the auroral breakup. In Fig. 5 where the data are sorted by MLT bins the earliest increase appears in panel 1 (01–04 MLT). This sector is to the dawnside of the average MLT location of the auroral onsets used in this study occurs. The (Liou et al., 2001) observed difference in local time between the injection and the auroral breakup location is smaller than that observed in this study, but observations of disperionsless injections farther than 1 h in local time from the auroral onset location have been observed before (Weygand et al., 2008). However, it is difficult to comment with any certainty in the difference in MLT location of the injection due to the large uncertainties and minimal number of events. When the proton flux injections are binned according to MLT the earliest injection appears to be in the 22–01 MLT bin. This sector is similar to the location of dipolarization observed by the GOES geosynchronous spacecraft (Cai et al., 2006) and the magnetic field line mapped location of the auroral onset observed with Viking auroral images (Elphinestone et al., 1991). Our location of the proton injection, however, is duskward of the mean location determined from the Polar ENA images of seven isolated substorm injections (Reeves and Henderson, 2001). Figs. 5 and 6 also seem to demonstrate the difference in location of the particle injections as discussed in Birn et al. (1997). These authors found that the region over which the proton injection occurs was shifted duskward with respect to the region over which the electron injection occurred.

For the ILT binned data the electron injection appears to start first in panel 8 of Fig. 6. If the start of the electron injection is at the minimum of the superposed epoch curve in the last panel, then the injection begins about 1–2 min after the auroral onset time and it occurred in the 22–01 ILT sector at the geosynchronous orbit. This observation agrees with the generally accepted view that the injection occurs after the auroral break up (Kremser et al., 1988; Liou et al., 2001). Panel 1 and possibly panel 2 also show an electron injection feature, but the decrease in the fluxes in panel 2 is less pronounced and the increase is not as large as the increase in panels 8 and 1. Panel 1 shows an increase in the electron fluxes also about 2 min after the auroral onset. The delayed injections observed in the other ILT bins are most likely due to a propagation effect.

The exact start of the increase of the proton fluxes in Fig. 6 is similar to that of the electron injection start time. The increase in the fluxes can be seen in panels 7 and 8. The proton flux increase in panel 7 (19–22 ILT) appears to begin about the same time as the auroral onset. In panel 8 the proton flux increase seems to begin about 2 min after the auroral onset. We believe that the proton injection begins in the 19–22 ILT sector, while the electron flux increase appears to begin in the 22–01 ILT sector.

Fig. 7 and Table 1 provide additional information that may help identify why the initial electron and proton fluxes increase at different times in Figs. 5 and 6. Fig. 7 is the histogram of the differences between the dispersionless particle injection and the auroral onset. In general the distributions are well defined, but the top two panels show one event where the dispersionless injection appears to begin well before the auroral onset. It is likely that this injection is not related to the auroral onset. The wide spread of the time differences and the paucity of events are reflected in the error of the mean given for the mean times in Table 1. What we can conclude from Table 1, Fig. 6 with the ILT bins, and Fig. 7 with the histograms is that dispersionless injection for our events begins at approximately the same time as the auroral onset within the error of the means and the cadence of the images. This observation of the similarity of the start time in the dispersionless injection and auroral onset in Table 1, Figs. 6 and 7 is consistent with the Liou et al. (2001) observation of the delayed injection relative to the auroral breakup as they observed for some of their events. Liou et al. (2001) determined that on average the injection is delayed about 1.8 ± 2.5 min after the auroral breakup and they attribute the delay to a propagation effect.

Timing studies, such as this one and others discussed here, are critical for evaluating current substorm models. The two most prominent models are the current disruption model, where the substorm is the result of the partial disruption of cross tail current along magnetic field lines into the auroral ionosphere (Liu et al., 1988), and the near earth neutral line model, where the substorm is the result of reconnection in the plasma sheet (Baker et al., 1996). A detailed discussion of the sequence of events that occur in the models is given in Angelopoulos (2008). For the current disruption model the Angelopoulos study indicates that the substorm current wedge forms sometime between the initial current disruption and the auroral breakup about 30 s later, then reconnection followed by the dispersionless injection begins 30 s after the auroral breakup. In the near earth neutral line model current disruption starts about 90 s after the initial reconnection, then the auroral breakup starts about 30 s after the current disruption. In this model the dispersionless injection begins just after reconnection and the current wedge also forms between the current disruption and the auroral breakup. Unfortunately, the results of our IL study do not clearly distinguish one model from the other. Our study suggests that the IL decrease observed in the histogram in Fig. 3 occurs on average 1 min before the

auroral onset in the IL histogram and the dispersionless injection begins about 0–4 min after the auroral onset in the histograms in Fig. 7. If we ignore the uncertainties in the time associated with the start of the IL decrease, auroral onset, and dispersionless injection, then the order of these events is the same as the current disruption model. However, the uncertainties in the IL decrease time, auroral onset time, and the dispersionless injection time make it impossible to support one model over the other. Future studies using the THEMIS ground magnetometers and auroral imagers should provide better determination of the time difference.

This study places the substorm onset time determined from the IL index and dispersionless particle injections in context with other methods of identifying substorm onsets, specifically the auroral onset time. Our results for a moderate number of substorms suggest that the IL index decreases before the image auroral onset and the dispersionless injection begins at the same time or after the auroral onset. This behavior may not have been noticed in the past because no previous study utilized a local AL index calculated from an array of ground magnetometers located below the auroral onsets. We look forward to validation or rejection of these preliminary results using data acquired in the THEMIS mission, which should allow a much larger statistical study of similar events.

Acknowledgments

This work was supported by NASA Grant NNG05GE00G.We would like to thank Dr. S. Mende for providing the IMAGE auroral images to CDAWeb and CDAWeb for making those images available to the community. We thank the institutes who maintain the IMAGE magnetometer array especially the PI institution: the Finnish Meteorological Institute. We thank the PI of the IMAGE magnetometer array, Dr. A. Viljanen, for producing the IE indices computation code. We would also like to thank Dr. M.G. Henderson for providing the LANL/SOPA plots and Dr. L.L. Lyons, Dr. E. Zesta, Dr. V. Angelopoulos for their advice for evaluating this study. Dr. R.L. McPherron also thanks the NSF Center for Integrated Space Model (CISM) for support though a subcontract on Grant ATM-0120950 to LASP in Boulder, CO.

References

Angelopoulos, V., 2008. The THEMIS mission. Space Science Reviews, in press, doi:10.1007/s11214-008-9336-1.

Atkinson, G., 1967. An approximate flow equation for geomagnetic flux tubes and its application to polar substorms. Journal of Geophysical Research 72, 5373–5382.

Baker, D.N., Pulkkinen, T.I., Angelopoulos, V., Baumjohann, W., Mcpherron, R.L., 1996. Neutral line model of substorms: past results and present view. Journal of Geophysical Research 101, 12,975–13,010.

Birn, J., Thomsen, M.F., Borovsky, J.E., Reeves, G.D., McComes, D.J., Belian, R.D., 1997. Characteristic plasma properties during dispersionless substorm injections at geosynchronous orbit. Journal of Geophysical Research 102, 2309–2324.

Cai, X., Henderson, M.G., Clauer, C.R., 2006. A statistical study of magnetic depolarization for sawtooth events and isolated substorms at geosynchronous orbit with GOES data. Annales Geophysicae 24, 3481–3490.

Elphinestone, R.D., Murphree, J.S., Cogger, L.L., Hearn, D., Henderson, M.G., 1991. Observations of changes to the auroral distribution prior to substorm onset. Magnetospheric Substorms, 257–275 Geophysical Monograph 64, American Geophysical Union, Washington, DC.

Frey, H.U., Mende, S.B., 2006. Substorm onsets as observed by IMAGE-FUV. In: Substorms VIII: Proceedings of ICS8. University of Calgary Press, Calgary, pp. 71–75.

Frey, H.U., Mende, S.B., Angelopoulos, V., Donovan, E.F., 2004. Substorm onset observations by IMAGE-FUV. Journal of Geophysical Research 109, A10304.

Henderson, M.G., Murphree, J.S., Reeves, G.D., 1994. The activation of the dusk-side and the formation of north–south aligned structures during substorms. In: Kan, J.R., Craven, J.D., Akasofu, S.-I. (Eds.), Substorms 2: Proceedings of the Second International Conference on Substorms, March 7–11, 1994. University of Alaska at Fairbanks, Fairbanks, Alaska, Geophysical Institute, University of Alaska Fairbanks, Fairbanks, Alaska, p. 37.

Hsu, T.-S., McPherron, R.L., 2003. Occurrence frequencies of IMF triggered and nontriggered substorms. Journal of Geophysical Research 108, 1307.

Hsu, T.-S., McPherron, R.L., 2007. A statistical study of the relation of Pi 2 and plasma flows in the tail. Journal of Geophysical Research 112.

Kauristie, K., Pulkkinen, T.I., Pellinen, R.J., Opgenoorth, H.J., 1996. What can we tell about global auroral-electrojet activity from a single meridional magnetometer chain? Annales Geophysicae 14, 1177–1185.

Koskinen, H.E.J., Lopez, R.E., Pellinen, R.J., Pulkkinen, T.I., Baker, D.N., Bsinger, T., 1993. Pseudo breakup and substorm growth phase in the ionosphere and magnetosphere. Journal of Geophysical Research 98, 5801–5813.

Kremser, G., Korth, A., Ullaland, S.L., Perraut, S., Roux, A., Pedersen, A., Schmidt, R., Tanskanen, P., 1988. Field-aligned beams of energetic electrons, $16\,\mathrm{keV} < E < 80\,\mathrm{keV}$) observed at geosynchronous orbit at substorm onset. Journal of Geophysical Research 93, 14453–14464.

Liou, K., Meng, C.-I., Lui, A.T.Y., Newell, P.T., Brittnacher, M., Parks, G., Reeves, G.D., Anderson, R.R., Yumoto, K., 1999. One relative timing in substorm onset signatures. Journal of Geophysical Research 104, 22,807–22,817.

Liou, K., Meng, C.-I., Newell, P.T., Takahashi, K., Ohtani, S.-I., Lui, A.T.Y., Brittnacher, M., Parks, G., 2000. Evaluation of low-latitude Pi 2 pulsations as indicators of substorm onset using Polar Ultraviolet imagery. Journal of Geophysical Research 105, 2495–2505.

Liou, K., Meng, C.-I., Newell, P.T., Lui, A.T.Y., 2001. Particle injections with auroral expansions. Journal of Geophysical Research 106, 5873–5881.

Liou, K., Meng, C.-I., Lui, A.T.Y., Newell, P.T., Wing, S., 2002. Magnetic depolarization with substorm expansion onset. Journal of Geophysical Research 107, 1131.

Liou, K., Newell, P.T., Meng, C.-I., Wu, C.C., Lepping, R.P., 2003. Investigation of external triggering with polar ultraviolet imager observations. Journal of Geophysical Research 108, 1364–1377.

Liu, A.T.Y., Lopez, R.E., Krimigis, S.M., McEntire, R.W., Zanetti, L.J., Potemra, T.A., 1988. A case study of the magnetotail current sheet disruption and diversion. Geophysical Research Letters 7, 721.

McPherron, R.L., Russell, C.T., Aubry, M., 1973. Satellite studies of magnetospheric substorms on August 15, 1978, 9, Phenomenological model for substorms. Journal of Geophysical Research 78, 3131–3149.

McPherron, R.L., Terasawa, T., Nishida, A., 1986. Solar wind triggering of substorm expansion onset. Journal of Geomagnetism and Geoelectricity 38, 1089–1108.

Nakamura, R., Baker, D.N., Yamamoto, T., Belian, R.D., Bering, E.A., Benbrook, J.A., Theal, J.R., 1994. Particle and field signatures during pseudobreakup and major expansion onset. Journal of Geophysical Research 99, 207.

Pulkkinen, T.I., Baker, D.N., Wiltberger, M., Goodrich, C., Lopez, R.E., Lyon, G., 1998. Pseudobreakup and substorm onset: observations and MHD simulations compared. Journal of Geophysical Research 103, 14,847.

Reeves, G.D., 1997. What we know and what we don't know about substorm injections. Geospace Environment Modeling Workshop, Snowmass, Colorado.

Reeves, G.D., Henderson, M.G., 2001. The storm–substorm relationship: ion injections in geosynchronous measurements and composite neutral atom imagers. Journal of Geophysical Research 106, 5833–5844.

Reeves, G.D., Fritz, T.A., Cayton, T.E., Belian, R.D., 1990. Multi-satellite measurements of the substorm injection region. Geophysical Research Letters 17, 2015–2018.

Reeves, G.D., Kettmann, G., Fritz, T.A., Belian, R.D., 1992. Further investigation of the CDAW 7 substorm using geosynchronous particle data: multiple injections and their implications. Journal of Geophysical Research 97, 6417–6428.

Ridley, A.J., 2000. Estimations of the uncertainty in timing the relationship between magnetospheric and solar wind processes. Journal of Atmospheric and Solar Terrestrial Physics 62, 757–771.

Sakurai, T., Sato, T., 1976. Magnetic pulsation Pi 2 and substorm onset. Planetary and Space Science 24, 573.

Sergeev, V.A., Liou, K., Meng, C.-I., Newell, P.T., Brittnacher, M., Parks, G., Reeves, G.D., 1999. Development of auroral streamers in association with localized impulsive injections to the inner magnetotail. Geophysical Research Letters 26, 417–420.

Weimer, D.R., 2004. Correction to "predicting interplanetary magnetic field (IMF) propagation delay times using the minimum variance technique. Journal of Geophysical Research 109, A12104.

Weimer, D.R., Ober, D., Maynard, N.C., Burke, W.J., Collier, M.R., McComas, D.J., Ness, N.F., Smith, C.W., 2002. Variable time delays in the propagation of the interplanetary magnetic field. Journal of Geophysical Research 107.

Weimer, D.R., Ober, D.M., Maynard, N.C., Collier, M.R., McComas, D.J., Ness, N.F., Smith, C.W., Watermann, J., 2003. Predicting interplanetary magnetic field (IMF) propagation delay times using the minimum variance technique. Journal of Geophysical Research 108, 1026.

Weygand, J.M., McPherron, R.L., Frey, H.U., Amm, O., Kauristie, K., Viljanen, A., Koistinen, A., 2008. Relation of substorm onset to Harang discontinuity. Journal of Geophysical Research, 113, A04213, doi:10.1029/2007JA012537.

Zesta, E., Donovan, E., Lyons, L., Enno, G., Murphree, J.S., Cogger, L., 2002. Two-dimensional structure of auroral poleward boundary intensifications. Journal of Geophysical Research 107, 1350.